ACS APPLIED ENERGY MATERIALS

www.acsaem.org Article

Assessment of Thermoelectric, Mechanical, and Microstructural Reinforcement Properties of Graphene-Mixed Heterostructures

Sadeq Hooshmand Zaferani, Reza Ghomashchi,* and Daryoosh Vashaee*

Cite This: *ACS Appl. Energy Mater.* 2021, 4, 3573−3583

Read Online

ACCESS | Metrics & More | Article Recommendations | Supporting Information

ABSTRACT: We examine the role of graphene nanoplates (GNPs) in the critical properties of thermoelectric GNP nanocomposites. After a detailed analysis of the thermoelectric, microstructural, and mechanical characteristics of such nanocomposites, we present a case study based on CoVSn-GNP heterostructures. It is shown that GNPs can improve the mechanical properties without deteriorating the thermoelectric properties of the material. CoVSn-GNP bulk composites are fabricated using powder metallurgy and spark plasma sintering with a GNP weight percentage range of 0−1. All samples with the addition of GNPs showed improved mechanical properties compared with pristine CoVSn. The sample with 0.5 wt % GNPs showed the highest value of Vickers Hardness (737 HV) among all of the studied compositions. Moreover, the fracture toughness was higher for the samples with a lower average crystal size. The concentration and dispersion of GNPs did not significantly change the CoVSn multiphase microstructure; however, it influenced the thermoelectric factors by reducing the thermal conductivity and increasing the Seebeck coefficient, leading to the enhancement of the thermoelectric figure of merit.

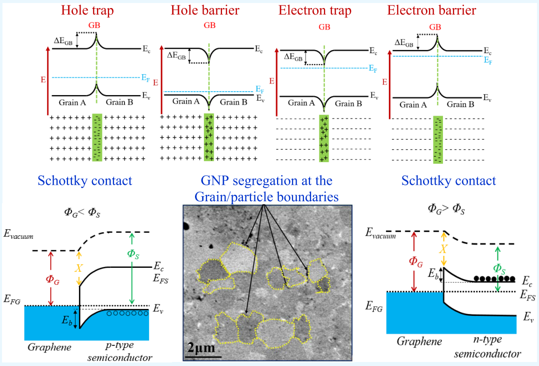

KEYWORDS: *graphene nanoplates, heterostructure composition, thermoelectrics, nanostructuring, CoVSn*

1. INTRODUCTION

To date, graphene-based nanomaterials have demonstrated remarkable characteristics in diverse applications such as the electronic,[1,2] biomedical,[3,4] coating,[5,6] and food industries.[7,8] Encouraged by such interesting findings, graphene compounds, such as few-layer graphene (FLG) and reduced graphene oxide (RGO), were also tested to modify the efficiencies of thermoelectric (TE) compounds through microstructural manipulation of TE materials.[9−11] However, the outcome is more complicated because multilayer graphene (i.e., stacked single graphene layers) may not possess the same effect as the two-dimensional (2D) defect-free single-layer graphene.[12−14] The impact of graphene inclusion on TE factors is summarized in Figure 1 through the critical analysis of several studies. In this figure, we have presented the Seebeck coefficient (S), electrical conductivity (σ), and thermal conductivity ($\kappa = \kappa_l$ (lattice) + κ_e(electronic)) and their contribution to the unit-less parameter of the figure of merit ($zT = S^2\sigma/\kappa\ T$) for both pristine TE compounds and their graphene-reinforced compositions.

As shown in Figure 1, graphene compounds have been shown to have various impacts on thermoelectric products. In the following sections, the scientific and engineering aspects of graphene's effects on electrical and thermal transport and the mechanical properties of thermoelectric compounds are discussed.

1.1. Graphene Impact on the Thermoelectric Properties.

1.1.1. Seebeck Coefficient. The Seebeck coefficient of a degenerate semiconductor and the carrier mobility can be expressed by[24,25]

$$S = \frac{\pi^2}{3}\frac{k_B^2 T}{q}\left[\frac{\partial(\ln(\sigma(E)))}{\partial E}\right]_{E=E_f} = \frac{\pi^2 k_B^2 T}{3q}\left[\frac{1}{n}\frac{\partial n(E)}{\partial E} + \frac{1}{\mu}\frac{\partial \mu(E)}{\partial E}\right]_{E=E_f} \quad (1)$$

$$\mu(E) = q\tau(E)/m_d^* \quad (2)$$

where E is the energy, $n(E)$ stands for the energy-dependent carrier density, and m_d^* is the effective mass of the charge carrier, while n, μ, q, K_B, E_f, and τ are the carrier concentration, carrier mobility, carrier charge, Boltzmann constant, Fermi energy, and charge carrier relaxation time, respectively. Assuming a parabolic energy band and the dependency of the relaxation time (τ) on the energy and the

Received: January 3, 2021
Accepted: March 11, 2021
Published: April 6, 2021

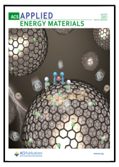

https://dx.doi.org/10.1021/acsaem.1c00015
ACS Appl. Energy Mater. 2021, 4, 3573−3583

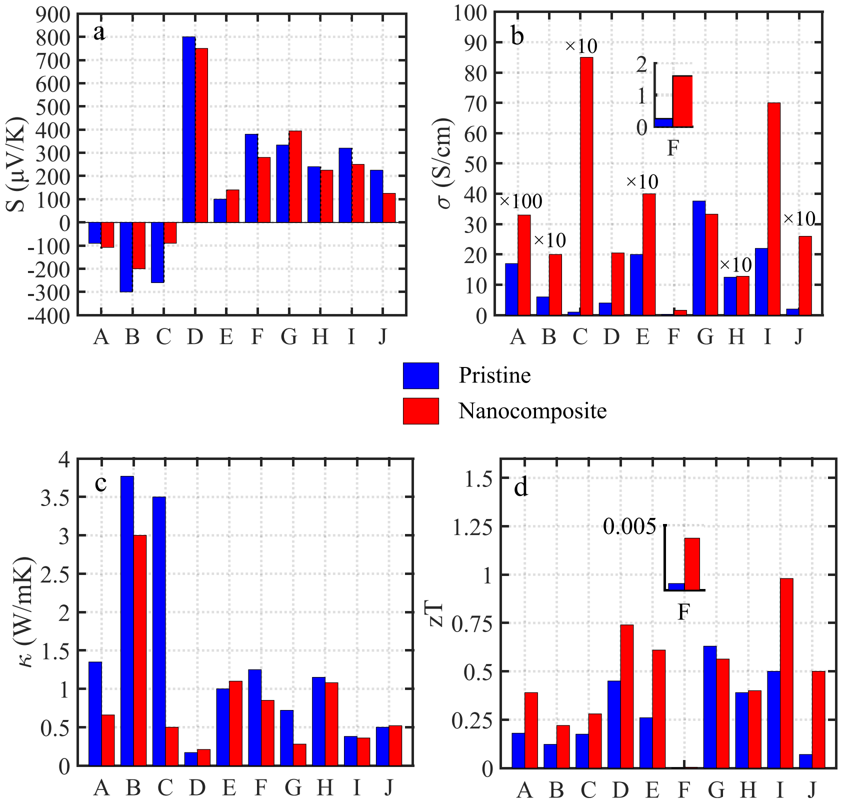

Figure 1. TE characteristics of pristine and graphene-reinforced nanocomposites, (a) Seebeck coefficients, (b) electrical conductivities, (c) lattice thermal conductivity (E and H show the total thermal conductivity), and (d) dimensionless figure of merit (zT): (A) $Bi_{0.85}Sb_{0.15}$-0.5 wt %G (T = 280 K),[15] (B) Nb-doped $SrTiO_3$-RGO (T = 800 K),[16] (C) $Zn_{0.98}Al_{0.02}O$-1.5 wt %RGO (T = 900 °C),[17] (D) *p*-phenediamino-modified graphene (PDG) (RT),[18] (E) $CoSb_3$/G (T = 800 K),[19] (F) $LaCoO_3$-0.01 wt % G (T = 300 K),[20] (G) MnTe-GNPs (T = 823 K),[21] (H) $CuInTe_2$/G (80:1) mass ratio (T = 700 K),[22] (I) SnSe-3.2 wt % MoS_2/G (T = 810 K).[23]

scattering factor (λ) via ($\tau = \tau_0 E^{\lambda}$) ($\tau_0$ is an energy-independent constant),[24,25] eq 1 can be written as[25]

$$S \approx \frac{\pi^2 k_B^2 T}{3q}\left[\frac{N(E)}{n} + \frac{\lambda}{Ef}\right]_{E=E_f} \tag{3}$$

where $N(E)$ is the electronic density of states. According to eq 3, the Seebeck coefficient depends directly on the scattering factor (λ) and is inversely affected by the charge carriers' concentration if the other parameters remain unchanged. It is well established that graphene reinforcement and its segregation at the grain boundaries (GBs) can lead to a grain size reduction in nanocomposites, when compared with a pristine matrix, by preventing welding or grain growth during milling and sintering, respectively.[9,21,22] The electrical characteristics of the sample with a single crystal and a polycrystalline structure may differ due to the effect of the grain/crystal boundaries.[26] However, the impact of the grain boundaries on the scattering of carriers is significant in case the mean free length (l) of carriers is larger than or comparable with the crystal/grain size (d).[26] The intrinsic tendency for carrier localization is created due to the presence of energetic disorder, caused by structural inhomogeneity and chemical impurities at the grain boundaries.[27,28] At the grain/crystal boundaries, this atomic disorder may provide electrical charge potential barriers (scattering regions) or traps.[27,28] The reason for this phenomenon is that the atoms near GBs are usually distributed irregularly, so the electronic couplings between atoms in different grains may change and thus prevent/disrupt the charge carriers' transport from one grain to the other.[29] This process can create traps, which may be classified as valleys (i.e., lower energy states) or barriers (i.e., higher energy states) by considering their energetic position with respect to the transport level.[30,31]

As shown in Figure 2, four scenarios may occur at the grain boundaries by considering the disturbed carrier concentration in these areas. If the structural inhomogeneity of the lattice at the grain boundaries creates electron donors near the valence-band maximum (VBM), hole traps are made (Figure 2a). Conversely, electron acceptors near the VBM act as dopants, making a barrier for holes[32,33] (Figure 2b). Similar behaviors apply to the cognitive bias modification (CBM).[33,34] The electron acceptors make a trap for electrons (Figure 2c), while the electron donors create a barrier for electrons (Figure 2d).[33,34]

There are further effects from the inclusion of graphene due to the formation of various lattice defects such as vacancies, antisites, etc., some of which can introduce extra charge carriers or compensate some of the donors or acceptors in the lattice.[38,39] However, in the case of graphene segregation, there are some other questions that need to be clarified, such as how the newly created graphene-matrix interfaces can affect electrical transport. The effect of graphene segregation at the grain interfaces can be evaluated, based on the possible band alignment, depending on the work functions of graphene and the main matrix. As illustrated in Figure 3, the type of contact (Schottky or

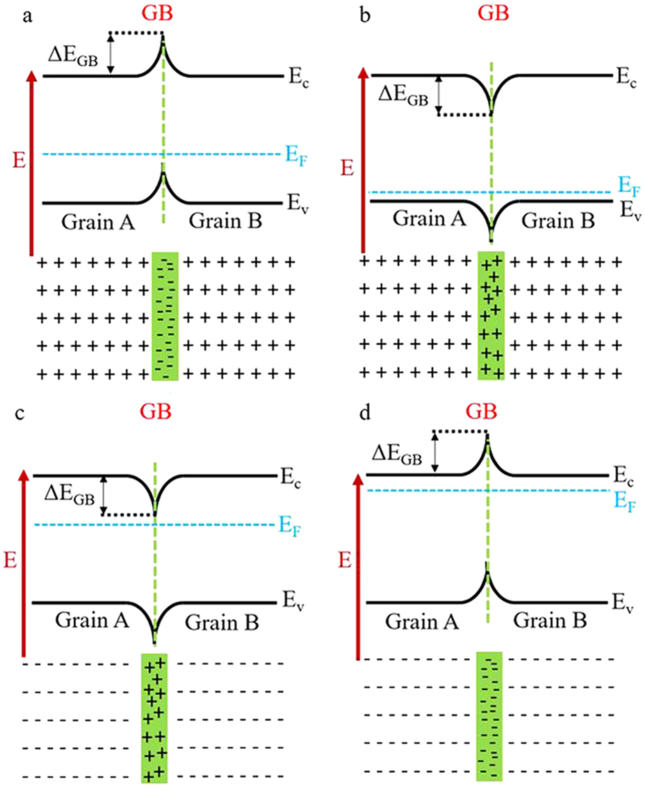

Figure 2. Schematic diagrams of (a) hole trap, (b) hole barrier, (c) electron trap, and (d) electron barrier. Adapted from ref 35−37.

ohmic) at the graphene-matrix interfaces depends on the type of the majority carriers in the matrix: electrons or holes. As shown in Figure 3, Schottky barriers occur at the graphene-matrix interfaces for both n- and p-type semiconductors when the graphene work function (Φ_G) is larger and smaller than the semiconductor work function (Φ_S), respectively (Figure 3a,b). In this case, there is an interface potential barrier (E_b), which scatters the low energy carriers preferentially more than the others, resulting in carrier energy filtering. In contrast, for the ohmic contact, there is no potential barrier, and all of the carriers can pass the interface (Figure 3c,d), although they can still experience scatterings due to potential energy variations at the interface.

Therefore, these extra boundaries due to smaller grain sizes—caused by graphene segregation and grain growth blocking—and graphene-matrix interfaces may provide an energy filtering effect for the charge carriers (electrons or holes). The consequence of energy filtering is the strong scattering of the low energy carriers, leading to reduced electrical conductivity and simultaneously increasing the Seebeck coefficient.[40,41]

1.1.2. Electrical Conductivity. The addition of graphene to the TE materials can result in either an increase or a decrease in the electrical conductivity (Figure 1b). This is due to graphene manipulating either the carrier concentration (n) or the mobility (μ), according to the Mott equation $\sigma = en\mu$.[9,22,38] The higher or lower carrier concentration depends on how graphene affects the crystal imperfections and interacts with the charge-donating centers in the material.[42,43] The graphene-embedded compounds may introduce a larger carrier concentration, but the resultant nanostructuring (i.e., grain growth prevention) provides more grain boundary barriers and thus further charge carrier scattering, leading to a decrease in the carrier mobility.[15,22] Therefore, one must consider both the carrier mobility of the matrix (μ_m) and the associated one to the interface (μ_{in}) to estimate the total mobility of the nanocomposites (eq 4),[38,44]

$$\frac{1}{\mu_T} = \frac{1}{\mu_m} + \frac{1}{\mu_{in}} \tag{4}$$

There are various models and approximations for interface mobility. One approximation is given by[38,44]

$$\mu_{in} = L_q\left(\frac{1}{2\pi m^* k_B T}\right)^{0.5} \exp\left(-\frac{E_b}{k_B T}\right) \tag{5}$$

where L_q is the mean path between two adjacent potential barriers, E_b shows the height of the potentials (energy) at the interfaces (Figure 3a,b), k_B is the Boltzmann constant, m^* is the effective mass of the charge carriers, and T is the absolute temperature.

1.1.3. Lattice Thermal Conductivity. Figure 1c shows that the addition of graphene in all of the listed materials reduces the lattice thermal conductivity. The primary mechanism is expected to be the phonon scattering against the grain boundaries,[22] which happens effectively at the low to medium temperature range.[45] Based on Matthiessen's rule,[45,46] the total relaxation time of phonons, τ_c (eq 6) is related to various relaxation times, including τ_U (Umklapp), τ_N (normal), $\tau_{e\text{-}ph}$ (electron phonon), τ_{pd} (point defect), $\tau_{i\text{-}ph}$ (impurity phonon), τ_{Ref} (regular reflection and refraction), τ_{Diff} (diffusive scattering due to the corrugation of the GB), and τ_{Ray} (Rayleigh scattering), as follows

$$\frac{1}{\tau_c} = \frac{1}{\tau_U} + \frac{1}{\tau_N} + \frac{1}{\tau_{e-ph}} + \frac{1}{\tau_{pd}} + \frac{1}{\tau_{i-ph}} + \frac{1}{\tau_{Ref}} + \frac{1}{\tau_{Diff}} + \frac{1}{\tau_{Ray}} \tag{6}$$

in which τ_{Ref}, τ_{Diff}, and τ_{Ray} depend on the grain boundary scattering, as described in Table 1.

It is noteworthy that graphene compounds can contribute to the electronic thermal conductivity ($\kappa = \kappa_e + \kappa_l$), based on the Wiedemann−Franz law (κ_e: $L\sigma T$, L: Lorentz number), the relationship that maps the electrical conductivity to the electronic thermal conductivity (κ_e).[47] In the cases where the electrical conductivity increases significantly, there may be a tradeoff between the increase of the electronic and reduction of the lattice thermal conductivities to determine the effect of graphene on the total thermal conductivity.[48]

Li et al.[49] obtained a significant reduction in thermal conductivity (from ∼0.8 to ∼0.4 W m^{-1} K^{-1} at a temperature of 873 K) by adding 0.15 wt % graphene in the Cu_2Se matrix. The reduction of the lattice thermal conductivity was associated with a frequency mismatch in the phonon density of states between carbon honeycomb phases and cubic Cu_2Se. Another study[50] reported a thermal conductivity of 2.5 W m^{-1} K^{-1} for a 0.25 vol % graphene/Cu_2SnSe_3 compound at room temperature, which was 12% lower than that of pristine Cu_2SnSe_3. In this study, the extra barriers created by the addition of graphene were mentioned as the reason for the phonon scattering and the reduction of the thermal conductivity of the nanocomposites.

1.2. Graphene's Mechanical Reinforcing Criteria.

1.2.1. Grain Refining. Grain refinement, through graphene

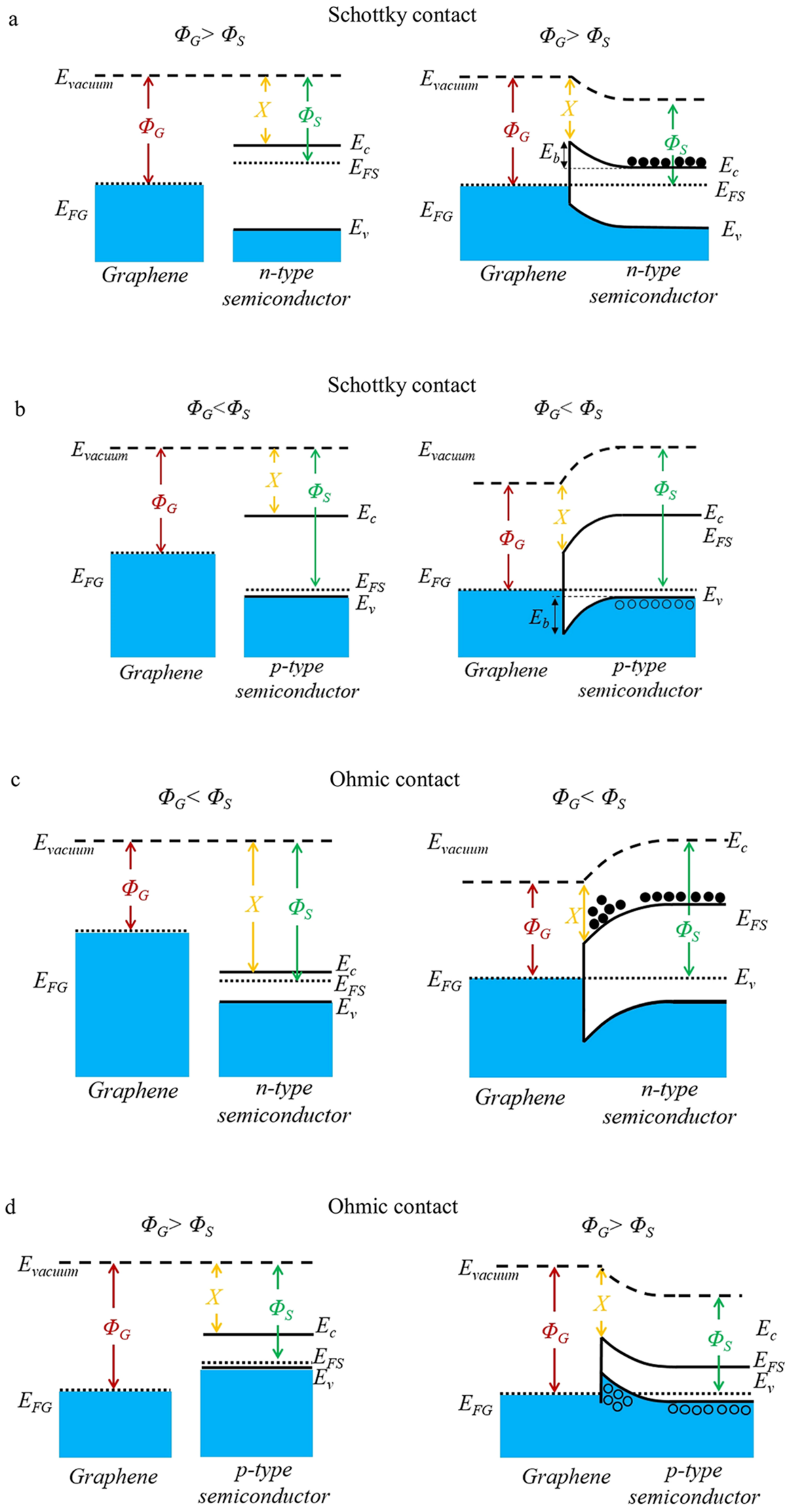

Figure 3. Schematic diagram of various contacts and band alignments at the graphene-matrix interface, (a) Schottky contact for graphene/n-type semiconductor, (b) Schottky contact for graphene/p-type semiconductor, (c) Ohmic contact for graphene/n-type semiconductor, and (d) ohmic contact for graphene/p-type semiconductor.

decoration of the grains, has been suggested as an effective method to improve the mechanical characteristics of nanocomposites.[51,52] Graphene addition to many granular alloys, due to graphene segregation at the grain/particle boundaries, inhibits the grain growth during the sintering process. In this regard, the Hall−Petch criteria explain the

Table 1. Phonon Scattering Strategies against the Grain Boundaries[45]

scattering strategies	parameters and relations	parameters	definitions
GB regular reflection and refraction	$\tau_{\mathrm{Ref}} \sim l_{\mathrm{GB}} v_{\mathrm{gj}}^{-1} (\Delta\nu)^{-2}$	l_{GB}	mean distance of the GBs
GB diffusive scattering	$\tau_{\mathrm{Diff}} \sim l_{\mathrm{GB}} v_{\mathrm{gj}}^{-1} \left(\frac{k_B \theta_j}{\hbar\omega}\right)^2 \frac{1}{\eta}$	v_{gj}	group velocity for the corresponding phonon modes
GB Rayleigh scattering	$\tau_{\mathrm{Ray}} \sim \left(\frac{v_{\mathrm{gj}}}{l_{\mathrm{GB}}}\right)^3 \left(\frac{\theta_j}{T\omega}\right)^4 \Xi$	$\Delta\nu$	difference in the refraction indices of the elastic waves in different grains
		k_B	Boltzmann constant
		θ_j	Debye temperature
		η	a parameter that characterizes the degree of the corrugation of the GB (typically $1 \ll 10$)
		$\hbar$	($\hbar = h/2\pi$), h is Plank's constant
		ω	phonon frequency
		Ξ	a constant, dependent on the details of the grain boundary characteristics
		T	absolute temperature

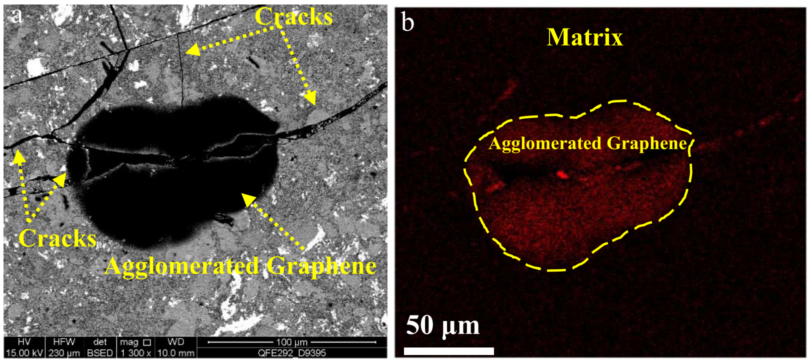

Figure 4. Graphene nanoplate (GNP) agglomeration at CoVSn- 1 wt % GNPs: (a) backscattered electron image and (b) carbon X-ray map.

manipulation of mechanical factors, specifically yield strength and hardness by grain size (d) reduction as follows[53,54]

$$\sigma_y = \sigma_0 + \frac{K_\sigma}{\sqrt{d}} \tag{7}$$

$$H = H_0 + \frac{K_{\mathrm{H}}}{\sqrt{d}} \tag{8}$$

where σ_y and H are the yield strength and hardness when grain growth is prevented by the reinforced GNPs, respectively; also, K_σ, K_{H} (slope of the straight line when σ_y or H is plotted against $1/\sqrt{d}$), H_0, and σ_0 are materials constants (friction stress opposing the motion of dislocation).

Furthermore, geometry mismatch may result from the presence of nonreacting graphene/matrix interfaces. The existence of an inharmonious geometry among the graphene segregates at the grain boundaries and within the grains can pin down the dislocations and thus strengthen the nanocomposites.[55]

In the graphene-reinforced alloys, several regions are the potential stress concentration/accumulations in the proximity of graphene nanoplates (GNPs) due to their high specific interface areas with the matrix. Accordingly, this factor can obstruct the dislocation movement and lead to mechanical stabilities in the nanocomposite.[56] It is noteworthy that the abovementioned phenomenon can be observed in the optimum reinforcing percentage and distribution of GNPs.[57] In this regard, Figure 4 illustrates how the agglomerated graphene nanoplates at the alloy matrix (a CoVSn compound in this figure) may not be able to prevent the crack growth or even create a crack. This issue emphasizes the importance of optimization of the graphene-mixing ratio to achieve a uniform distribution.

Equation 9 calculates the strengthening efficiency of reinforcement (R),[51] based on the strengths of the composite (σ_c), matrix (σ_m), and reinforcement volume fraction (V_r).

$$R = \frac{\sigma_c - \sigma_m}{V_r \sigma_m} \tag{9}$$

Based on this equation, increasing the reinforcement volume above the optimum value may not enhance the reinforced strength, as illustrated in Figure 4.

1.2.2. Load Transferring.

1.2.2. Load Transferring. Three main factors control the load transfer mechanism in the nanocomposites, namely, the reinforcement geometry, volume fraction, and bonding strength among the matrices and nanofillers.[51] By reinforcing a matrix with GNPs, the tight bonding (interlocking) due to the large interface areas of the GNPs/matrix enhances the load transfer between graphene and the matrices.[51] The formation of strong bonding was reported by Bhadauria et al.[55] through the transmission electron microscopy (TEM) analysis of the interface (Figure 5a). The results revealed a clean interface with good metallurgical bonding between GNP reinforcement and the Al matrix, which can improve the load transfer between graphene and the matrix. The high-resolution TEM image of the interface region, illustrated in Figure 5b, reveals the nature of the bonding between graphene and the Al matrix.

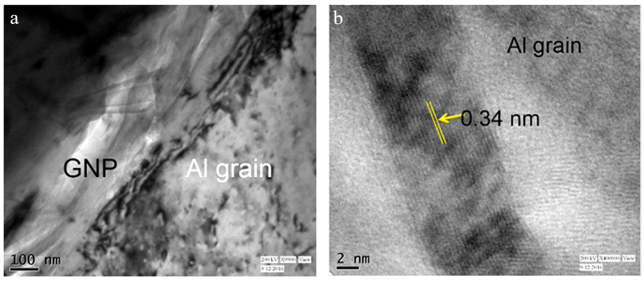

Figure 5. (a) TEM micrographs showing the Al−GNP interface and (b) high-resolution TEM image showing graphene layers in the GNP, along with its interface structure with an Al matrix.[55]

In this case, eq 10 can estimate the nanocomposite strength via the volume fraction and interfacial areas[58]

$$\sigma_{\text{nanocomposite}} = V_r\left(\frac{A}{CS}\right)\left(\frac{\tau}{2}\right) + \sigma_m V_m \tag{10}$$

where V_r shows the reinforcement's volume fraction, A and CS are interfacial surfaces and cross sections of reinforcements, respectively, τ stands for shear stress; σ_m is the matrix strength, and V_m is the matrix volume fraction. According to this equation, for the optimum dispersed GNPs in the matrix, the interfacial surface area (A) increases and the reinforcement's cross section (CS) decreases, which leads to an enhancement of the nanocomposite strength. In other words, the matrix reinforced by GNPs provides more effective interfaces and facilitates the load transfer from the matrices into GNPs via shear stress.[53] This mechanism causes load distribution and enables the strong reinforcing agent (GNPs) to take most of the applied load and prevent any local stress concentrations in the matrix and any subsequent premature nanocomposite failure.

1.2.3. Thermal Expansion Coefficient Mismatch. Dislocation can be generated due to the differences in the thermal expansion coefficients (TECs) contributed to matrices and GNPs.

Equation 11 describes the effective parameters in strength improvement, based on the TEC differences between the matrix and GNPs[59]

$$\sigma_{\text{TEC}} = \alpha G b\sqrt{\frac{12\Delta T\Delta C}{bd}} \tag{11}$$

where α is a constant, G shows the shear modulus, b represents the magnitude of the Burgers vector, ΔT is the temperature gradient between the process and the ambient, ΔC states the TEC difference, and d is the particle size.

As shown in this equation, the residual stress creation due to the TEC difference is directly related to ΔC. Moreover, the mismatch in the TECs is caused by residual stress.[60]

Equation 12 estimates the change in strength based on the density of the dislocations. In this equation, α is the geometric constant, μ_m shows the matrix shear modulus, b represents the Burgers vector magnitude, and ρ is the dislocation density.[60]

$$\Delta\sigma = \alpha\mu_m b\sqrt{\rho} \tag{12}$$

As represented in this equation, well-dispersed GNPs with a high level of interface areas with the matrix generate a higher density of dislocations and residual stress.

1.2.4. Orowan and Griffith Criteria. Orowan reinforcement is another mechanism that has been evaluated for reinforcing the matrix using GNPs. In this process, graphene may cause the pile-up of the dislocations and prevent them from moving freely throughout the matrix. Consequently, the dislocations need to pass around the graphene nanoplates due to their high mechanical stability. This extension in the dislocation paths (loops) results in higher ductility for the nanocomposites. Furthermore, these loops can create back stresses and prevent dislocation motions.[55] Equation 13[59] describes the strength regarding this mechanism, based on the effective parameters, such as

$$\sigma_o = \frac{Gb}{2\pi\sqrt{1-\frac{\theta}{1.28}\left[\frac{1}{\sqrt{V_r}}-1\right]}\,d}\ln\frac{d}{1.27b} \tag{13}$$

where G states the shear modulus, b is the Burgers vector magnitude, θ is Poisson's ratio, V_r is the reinforcement volume fraction, and d is the particle size.

Candidate thermoelectric materials for waste heat recovery applications such as heavily doped semiconductors and ceramic oxides are predominately brittle materials.[61] By considering this critical feature, the performance of the GNPs in strengthening the thermoelectric compounds against brittle fracture can be estimated via Griffith's fracture criterion (eq 14). In this equation, the critical stress intensity factor ($K_c = \sigma_c\sqrt{\pi a_0}$) depends on Young's modulus (E) and surface energy (γ) (i.e., the edge energy for 2D materials like graphene).

$$K_c = \sigma_c\sqrt{\pi a_0} = \sqrt{2\gamma E} \tag{14}$$

where a_0 stands for the half crack length and σ_c shows the critical stress at the fracture onset.[62]

Nevertheless, there is a crack length restriction (up to 10 nm) when using the Griffith criterion,[63] but as per an

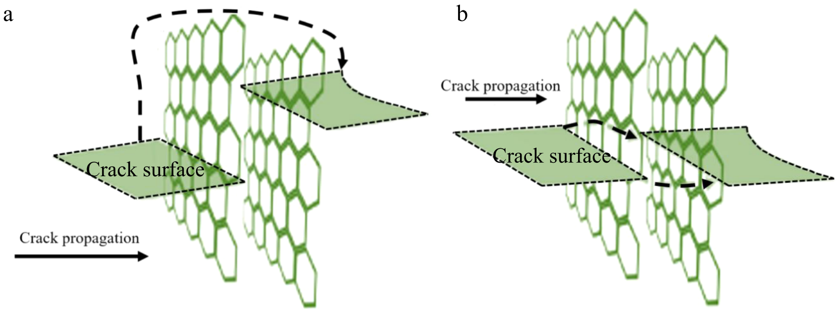

Figure 6. Schematic of crack growth inhibition by (a) crack deflection and (b) crack bifurcation/pinning, adapted from ref 65 with permission.

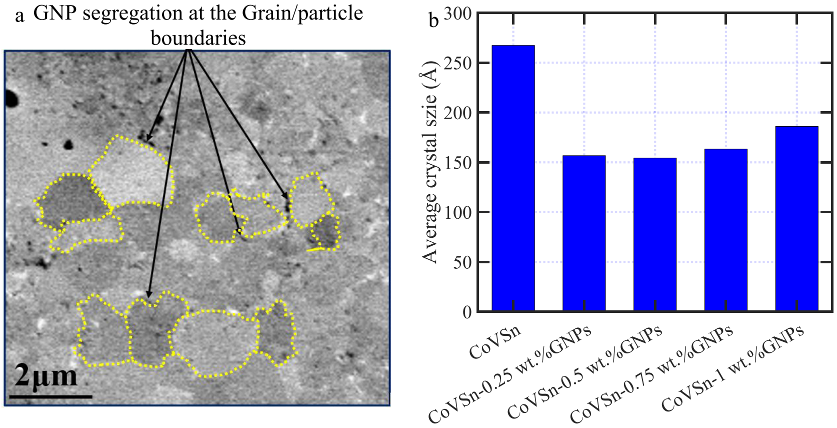

Figure 7. (a) GNP segregation at the grain/particle boundaries and (b) average crystal size of CoVSn heterostructure compositions.

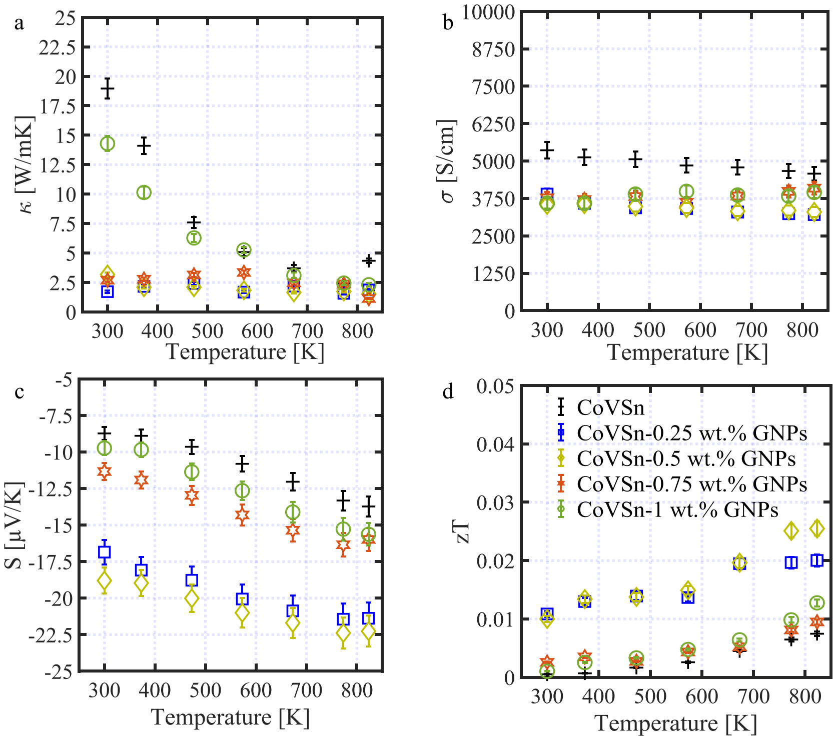

Figure 8. Temperature-dependent thermoelectric characteristics of CoVSn-GNP heterostructure compounds, (a) thermal conductivity, (b) electrical conductivity, (c) Seebeck coefficients, and (d) *zT*.

adequate dispersion of GNPs, these reinforcements with a high Young's modulus can improve the nanocomposite strength[64] and its resistance to crack propagation by improving the modulus (eq 14) as follows

$$\sigma_c = \sigma_{Gr}X_{Gr} + \sigma_m X_m \tag{15}$$

$$E_c = E_{Gr}X_{Gr} + E_m X_m \tag{16}$$

where E_c shows Young's modulus of the nanocomposites and E_{Gr}, E_m, X_{Gr}, and X_m are Young's moduli and volume fractions of the graphene nanoplates and the matrix, respectively.

Moreover, Figure 6 demonstrates schematically the crack growth blocking or halting by GNPs.

This process can also be interpreted based on eq 14, in which increasing the nanocomposite Young's modulus (*E*) and increasing K_c—fracture toughness—result in a lower crack propagation tendency.

In the following section, we report a case study on CoVSn and study the effect of graphene on the thermoelectric, microstructure, and mechanical properties of the nanocomposite structure. The CoVSn composition was studied in its pristine phase and presented in a prior publication.[66] Here, the heterogeneous composition is evaluated through reinforcement with graphene nanoplates.

2. MATERIALS AND METHODS

The synthesis of the CoVSn compound has been reported, and its multiphase composition and microstructure were discussed in an earlier work by the authors[66] (Figures S1 and S2). Here, the impacts of graphene nanoplate (GNP) reinforcement on the CoVSn microstructure and its properties are studied.

The CoVSn-xGNP (x: 0.25 wt % [0.047 atom %], 0.5 wt % [0.095 atom %], 0.75 wt % [0.142 atom %], and 1 wt % [0.19 atom %]) compounds were prepared using micromilling (reciprocating type, 1 h, a ball/powder volume ratio of 1:1, the stainless steel ball size of 1 mm) of the synthesized CoVSn powder with the GNPs (average particle: size 3 nm, surface area: 500 m^2 g^{-1}, Alfa Aesar) under an argon atmosphere. The bulk samples were fabricated with an average density (≈98 to 99% theoretical density measured by the Archimedes method, with isopropyl alcohol as a displacement medium) via spark plasma sintering (SPS) at a temperature of 850 °C and an applied pressure of 42 MPa, with a sintering time of 20 min under an argon atmosphere. The phase identification was implemented via X-ray diffraction (XRD) analysis (MiniFlex 300/600, 40 kV, 15 mA, Cu X-ray tube generation). Field emission scanning electron microscopy (FESEM) Quanta 450 SEM was employed for microstructural analysis. The Seebeck coefficient (S) and electrical conductivity (σ) were measured under a He environment at a temperature range of 300−820 K on a commercial Linseis LSR-3 system, using a differential voltage/temperature technique and a DC four-probe method, respectively. The thermal conductivity (κ) was calculated using $\kappa = D\rho C_P$ where ρ(g cm^{-3}) is the sample density. The thermal diffusivity D (m^2 s^{-1}) and specific heat capacity C_P (J Kg^{-1} K^{-1}) were measured with laser flash and differential scanning calorimetry methods, respectively, on Linseis LFA and DSC instruments, at a temperature range of 300−820 K. Moreover, the Vickers hardness values were measured using a microhardness device (LECO, LM-700AT-load: 1000 g, dwell time: 10 s) at room temperature.

3. RESULTS AND DISCUSSION

The segregation of GNPs at GBs in Figure 7 presents the range of the average crystal size of CoVSn-GNP heterostructure compounds estimated from the XRD analysis. The addition of GNPs has resulted in smaller crystallites, which are saturated at approximately 15−18 nm. The segregation of GNPs at the grain boundaries, creating new microstructural interfaces and providing extra boundaries, influenced the thermoelectric properties (Figure 8). The reduction in thermal conductivity is clearly illustrated in Figure 8a. Phonon scattering against the microstructural boundaries (grain/crystal boundaries and GNP distribution as a second phase) can be regarded as a reason for reducing the thermal conductivities. Based on the results, the primary reduction occurred at a lower temperature due to the main impact of phonon scattering with a longer wavelength (low frequencies) against the grain boundaries.[45]

Figure 8b shows the electrical conductivities of the samples after reinforcing with GNPs, which are in the range of conductive compounds. Moreover, Figure 8c illustrates the negative Seebeck coefficients for the samples to confirm the presence of electrons as the majority carriers. However, for the compounds with more than 0.5 wt % GNPs, there is a disruption in the improvement of the TE characteristics. This can be attributed to a lack of uniform GNP dispersion in the matrix and formation of the agglomerated GNP regions, as shown in Figure 9, which are also reported for other nanocomposites.[50,67]

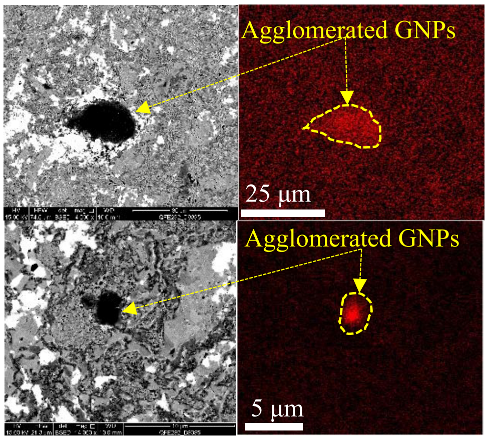

Figure 9. Backscattered electron micrographs with respective X-ray maps illustrating the GNP agglomerations in the matrix of the CoVSn-1 wt % GNPs nanocomposite.

Moreover, the microstructural analysis revealed multiphase microconstituents for the CoVSn-GNPs (e.g., CoVSn-1 wt % GNPs—Figure 10), similar to the pristine CoVSn sample, as discussed in ref 66 Figure 10 shows the elemental dispersion via X-ray mapping. It can be seen that the distributions of the main three elements, Co, V, and Sn, are not uniform, which confirms the presence of a multiphase microstructure. The comparison with the multiphase microstructure of the pristine CoVSn shows that the incorporation of GNPs does not influence the formation of the constituent phases in the microstructure (Figure S3).

Table 2 illustrates the hardness measurement results of the studied heterostructure compositions after reinforcement with the GNPs. The average hardness of the samples containing GNPs is higher than the pristine sample. This result can be explained by considering the presence of the GNPs as a second phase in the matrix and the smaller average crystal size—extra microstructural barriers (Hall−Petch effect[54]). In this regard, the dispersion of GNPs in the matrix is expected to hinder dislocation movements[68] and, consequently, strengthen the GNP-reinforced CoVSn heterostructure composition. It appears that the optimum concentration of GNPs to achieve the highest hardness is about 0.5%, and the further addition of GNPs reduces the hardness. Such an outcome may be attributed to the distribution of GNPs. A higher GNP concentration results in their agglomeration (Figure 9) and thus reduces the hardness.

Fracture toughness (K_{IC}, MPa$\sqrt{m}$) values were calculated based on the Shetty equation $K_{IC} = 0.0899\sqrt{\frac{HP}{4l}}$.[21] Here H, P, and l are the hardness, applied load of indentation, and indentation crack length, respectively. The average of the radial crack length was calculated from five indentations measured for each specimen (Figure 11). The calculations exhibit a higher fracture toughness for the sample containing 0.5 wt % GNPs (Table 2). This observation is attributable to halting the crack propagation against the extra microstructural interfaces/barriers, caused by the grain/crystal growth prevention (i.e., creating smaller grain/crystal sizes) in the graphene-reinforced CoVSn samples.

4. CONCLUSIONS

The scientific and engineering aspects of the graphene effects on mechanical, thermal, and electrical properties of thermoelectric materials were presented. The mechanisms under which GNPs affect the charge carrier concentration, carrier mobility, thermal conductivity, and thermopower were discussed. Special attention was paid to the incorporation of multilayer graphene as the reinforcing agent. As a case study, the impact of graphene nanoplates (GNPs) on the CoVSn heterostructure composition properties was analyzed.

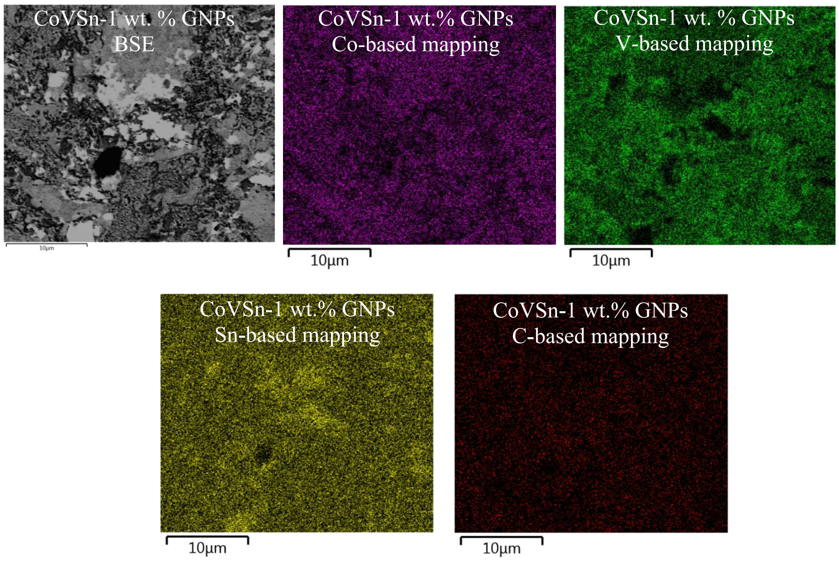

Figure 10. Backscattered electron micrograph along with X-ray maps showing the formation of multiphase microstructures in CoVSn-1 wt % GNPs.

Table 2. Mechanical Characteristics of the MnTe-GNP Samples

sample	CoVSn	CoVSn-0.25 wt % GNPs	CoVSn-0.5 wt % GNPs	CoVSn-0.75 wt % GNPs	CoVSn-1 wt % GNPs
hardness (HV)	592	636	737	695	682
SD: standard deviation	(SD: 15.3)	(SD: 17.2)	(SD: 12.4)	(SD: 16.7)	(SD: 12.6)
$K_{IC}(\mathrm{MPa}\sqrt{\mathrm{m}})$	1.954	1.980	2.277	1.982	1.957

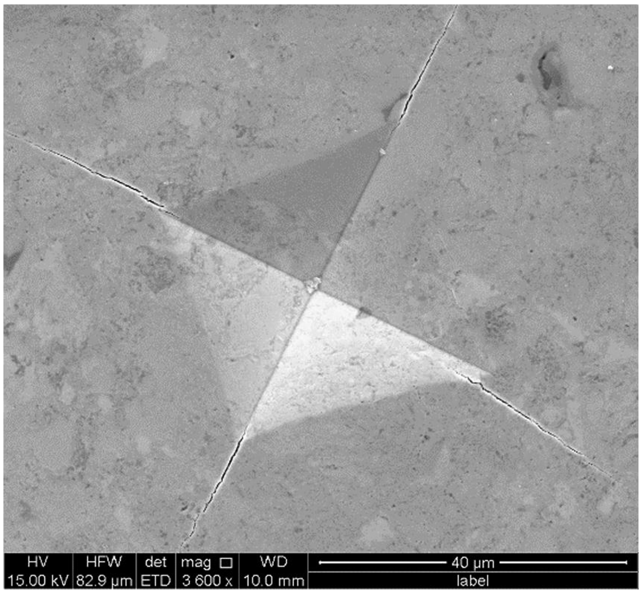

Figure 11. Crack length measurement to calculate the fracture toughness.

The mechanical assessment showed higher hardness (737 HV) in the sample reinforced with 0.5 wt % GNPs. This can be explained by the dispersion of the GNPs in the matrix and the excess microstructural barriers, due to small crystal sizes, hindering the dislocation movements and, consequently, strengthening the nanocomposite. The dispersion of GNPs did not significantly impact the CoVSn multiphase microstructure but enhanced the thermopower and reduced both the electrical and thermal conductivities. For some concentrations of the GNPs (0.25 and 0.5 wt %), zT was improved.

■ ASSOCIATED CONTENT

SI Supporting Information

The Supporting Information is available free of charge at https://pubs.acs.org/doi/10.1021/acsaem.1c00015.

> Isopleth phase diagram of CoVSn composition; XRD pattern of CoVSn composition; X-ray line mapping of CoVSn-GNP scomposites (PDF)

■ AUTHOR INFORMATION

Corresponding Authors

Reza Ghomashchi − *School of Mechanical Engineering, University of Adelaide, Adelaide, SA 5005, Australia; ARC Research Hub for Graphene Enabled Industry Transformation and Institute for Photonics And Advanced Sensing, University of Adelaide, Adelaide, SA 5005, Australia*; Email: reza.ghomashchi@adelaide.edu.au

Daryoosh Vashaee − *Department of Electrical and Computer Engineering and Department of Materials Science and Engineering, North Carolina State University, Raleigh, North Carolina 27606, United States*; orcid.org/0000-0003-3667-3672; Email: dvashae@ncsu.edu

Author

Sadeq Hooshmand Zaferani − *School of Mechanical Engineering, University of Adelaide, Adelaide, SA 5005, Australia; Department of Electrical and Computer Engineering, North Carolina State University, Raleigh, North Carolina 27606, United States*; orcid.org/0000-0001-8923-6762

Complete contact information is available at: https://pubs.acs.org/10.1021/acsaem.1c00015

Notes

The authors declare no competing financial interest.

■ ACKNOWLEDGMENTS

This work was supported by the Australian Government Research Training Program Scholarship and the ARC Graphene Enabled Industry Transformation Hub at the University of Adelaide. This study is partially based upon work supported by the Air Force Office of Scientific Research (AFOSR) under contract number FA9550-19-1-0363 and the National Science Foundation (NSF) under grant numbers ECCS-1351533, ECCS-1515005, and ECCS-1711253.

■ REFERENCES

(1) Schwierz, F. Graphene transistors. *Nat. Nanotechnol.* **2010**, *5*, 487−496.

(2) Yazyev, O. V.; Louie, S. G. Electronic transport in polycrystalline graphene. *Nat. Mater.* **2010**, *9*, 806−809.

(3) Syama, S.; Mohanan, P. V. Comprehensive Application of Graphene: Emphasis on Biomedical Concerns. *Nano-Micro Lett.* **2019**, *11*, No. 6.

(4) Bullock, C. J.; Bussy, C. Biocompatibility Considerations in the Design of Graphene Biomedical Materials. *Adv. Mater. Interfaces* **2019**, No. 1900229.

(5) Nine, M. J.; Kabiri, S.; Diana, T. T. T.; Tran, N. H.; Losic, D. Electrostatic powder coatings of pristine graphene: A new approach for coating of granular and fibril substrates. *Appl. Surf. Sci.* **2018**, *441*, 187−193.

(6) Nine, M. J.; Cole, M. A.; Tran, D. N. H.; Losic, D. Graphene: a multipurpose material for protective coatings. *J. Mater. Chem. A* **2015**, *3*, 12580−12602.

(7) Wang, M.; Cui, M.; Zhao, M.; Cao, H. Sensitive determination of Amaranth in foods using graphene nanomeshes. *J. Electroanal. Chem.* **2018**, *809*, 117−124.

(8) Goh, K.; Yuan, Y.; Karahan, H. E.; Wei, L.; Zhai, S.; Htin, N. M.; Rong, W.; Fane, A. G.; Dekker; M.:Dehghani, F.; Chen, Y.; et al. Sandwich-Architectured Poly(lactic acid)−Graphene Composite Food Packaging Films. *ACS Appl. Mater. Interfaces* **2016**, *8*, 9994−10004.

(9) Shin, W. H.; Ahn, K.; Jeong, M.; Yoon, J. S.; Song, J. M.; Lee, S.; Seo, W. S.; Lim, Y. S. Enhanced thermoelectric performance of reduced graphene oxide incorporated bismuth-antimony-telluride by lattice thermal conductivity reduction. *J. Alloys Compd.* **2017**, *718*, 342−348.

(10) Zong, P.-a.; Liang, J.; Zhang, P.; Wan, C.; Wang, Y.; Koumoto, K. Graphene-Based Thermoelectrics. *ACS Appl. Energy Mater* **2020**, *3*, 2224−2239.

(11) Chakraborty, P.; Ma, T.; Zahiri, A.; Cao, L.; Wang, Y. Carbon-Based Materials for Thermoelectrics. *Adv. Condens. Matter Phys.* **2018**, No. 3898479.

(12) Kakaei, K.; Esrafili, M. D.; Ehsani, A. Atomic Properties and Electronic Structure. In *Interface Science and Technology*, 2019; pp *27*, 23−66.

(13) Nilsson, J.; Castro Neto, A. H.; Guinea, F.; Peres, N. M. R. Electronic Properties of Graphene Multilayers. *Phys. Rev. Lett.* **2006**, *97*, No. 266801.

(14) Amollo, T. A.; Mola, G. T.; Kirui, M. S. K.; Nyamori, V. O. Stacking order dependent electric field tuning of the band gap in graphene multilayers. *Phys. Rev. B* **2010**, *81*, No. 115432.

(15) El-Asfoury, M. S.; Nasr, M.; Nakamura, K.; Abdel-Moneim, A. Enhanced thermoelectric performance of Bi85Sb15-graphene composite by modulation carrier transport and density of state effective mass. *J. Alloys Compd.* **2018**, *745*, 331−340.

(16) Wu, C.; Li, J.; Fan, Y.; Xing, J.; Gu, H.; Zhou, Z.; Lu, X.; Zhang, Q.; Wang, L.; Jiang, W. The effect of reduced graphene oxide on microstructure and thermoelectric properties of Nb-doped A-site-deficient SrTiO3 ceramics. *J. Alloys Compd.* **2019**, *786*, 884−893.

(17) Chen, D.; Zhao, Y.; Chen, Y.; Wang, B.; Chen, H.; Zhou, J.; Liang, Z. One-Step Chemical Synthesis of ZnO/Graphene Oxide Molecular Hybrids for High-Temperature Thermoelectric Applications. *ACS Appl. Mater. Interfaces* **2015**, *7*, 3224−3230.

(18) Lin, Y.-H.; Lee, T.; Hsiao, Y.; Lin, W.; Whang, W.; Chen, C. Facile Synthesis of Diamino-Modified Graphene/Polyaniline Semi-Interpenetrating Networks with Practical High Thermoelectric Performance. *ACS Appl. Mater. Interfaces* **2018**, *10*, 4946−4952.

(19) Feng, B.; Xie, J.; Cao, G.; Zhua, T.; Zhao, X. Enhanced thermoelectric properties of p-type CoSb3/graphene nanocomposite. *J. Mater. Chem. A.* **2013**, *1*, 13111−13119.

(20) Kumar, A.; Kumari, K.; Ray, S. J.; Thakur, A. D. Graphene mediated resistive switching and thermoelectric behavior in lanthanum cobaltate. *J. Appl. Phys.* **2020**, *127*, No. 235103.

(21) Hooshmand Zaferani, S.; Ghomashchi, R.; Vashaee, D. Thermoelectric, Magnetic, and Mechanical Characteristics of Antiferromagnetic Manganese Telluride Reinforced with Graphene Nanoplates. *Adv. Eng. Mater.* **2021**, *23*, No. 2000816.

(22) Chen, H.; Yang, C.; Liu, H.; Zhang, G.; Wan, D.; Huang, F. Thermoelectric properties of CuInTe2/graphene composites. *CrystEngComm* **2013**, *15*, 6648−6651.

(23) Yang, S.; Si, J. X.; Su, Q.; Wu, H. Enhanced thermoelectric performance of SnSe doped with layered MoS2/graphene. *Mater. Lett.* **2017**, *193*, 146−149.

(24) Heremans, J. P.; Thrush, C. M.; Morelli, D. T. Thermopower enhancement in PbTe with Pb precipitates. *J. Appl. Phys.* **2005**, *98*, No. 063703.

(25) Li, Y.; Dou, Y.; Qin, X.; Zhang, J.; Xin, H.; Li, D.; Song, C.; Zou, T.; Liu, Y.; Li, C. Enhanced thermoelectric figure of merit in p-type b-Zn4Sb3/Bi0.4Sb1.6Te3 nanocomposites. *RSC Adv.* **2016**, *6*, 12243−12248.

(26) Kaydanov, V. I.; Coutts, T. J.; Young, D. L. In *Studies of Band Structure and Free-Carrier Scattering in Transparent Conducting Oxides Based on Combined Measurements of Electron Transport Phenomena*, Presented at the Material Research Society Workshop Denver, Colorado June 19-20, 2000.

(27) Puntambekar, K.; Dong, J.; Haugstad, G.; Frisbie, C. D. Structural and Electrostatic Complexity at a Pentacene/Insulator Interface. *Adv. Funct. Mater.* **2006**, *16*, 879−884.

(28) Yogev, S.; Matsubara, R.; Nakamura, M.; Rosenwaks, Y. Local charge accumulation and trapping in grain boundaries of pentacene thin film transistors. *Org. Electron.* **2010**, *11*, 1729−1735.

(29) Nan, G.; Li, Z. Modeling of charge transport in polycrystalline sexithiophene from quantum charge transfer rate theory beyond the first-order perturbation. *Org. Electron.* **2011**, *12*, 2198−2206.

(30) Vladimirov, I.; Kühn, M.; Geßner, T.; May, F.; Weitz, R. T. Energy barriers at grain boundaries dominate charge carrier transport in an electron-conductive organic semiconductor. *Sci. Rep.* **2018**, *8*, No. 14868.

(31) Steiner, F.; Poelking, C.; Niedzialek, D.; Andrienko, D.; Nelson, J. Influence of orientation mismatch on charge transport across grain boundaries in tri-isopropylsilylethynyl (TIPS) pentacene thin films. *Phys. Chem. Chem. Phys.* **2017**, *19*, 10854−10862.

(32) Qian, C.; Sun, J.; Zhang, L.; Huang, H.; Yang, J.; Gao, Y. Crystal-Domain Orientation and Boundary in Highly Ordered Organic Semiconductor Thin Film. *J. Phys. Chem. C* **2015**, *119*, 14965−14971.

(33) Kaake, L. G.; Barbara, P. F.; Zhu, X.-Y. Intrinsic Charge Trapping in Organic and Polymeric Semiconductors: A Physical Chemistry Perspective. *J. Phys. Chem. Lett.* **2010**, *1*, 628−635.

(34) Baier, R.; Leendertz, C.; Abou-Ras, D.; Ch.Lux-Steiner, M.; Sadewasser, S. Properties of electronic potential barriers at grain boundaries in Cu(In,Ga)Se2 thin films. *Sol. Energy Mater. Sol. Cells* **2014**, *130*, 124−131.

(35) Seto, J. Y. W. The electrical properties of polycrystalline silicon films. *J. Appl. Phys.* **1975**, *46*, 5247.

(36) Kamins, T. Hall Mobility in Chemically Deposited Polycrystalline Silicon. *J. Appl. Phys.* **1971**, 4357−4365.

(37) Grovenor, C. R. M. Grain boundaries in semiconductors. *J. Phys. C: Solid State Phys.* **1985**, *18*, 4079.

(38) Li, C.; Qin, X.; Yuanyue Li, Y.; Li, D.; Zhang, J.; Guo, H.; Xin, H.; Song, C. Simultaneous increase in conductivity and phonon scattering in a graphene nanosheets/(Bi2Te3)0.2(Sb2Te3)0.8 thermoelectric nanocomposite. *J. Alloys Compd.* **2016**, *661*, 389−395.

(39) Lu, M.-P.; Liao, C.-N. Mechanical and thermal processing effects on crystal defects and thermoelectric transport properties of Bi2(Se,Te)3 compounds. *J. Alloys Compd.* **2013**, *571*, 178−182.

(40) Paul, B.; Kumar, V. A.; Banerji, P. Embedded Ag-rich nanodots in PbTe: Enhancement of thermoelectric properties through energy filtering of the carriers. *J. Appl. Phys.* **2010**, *108*, No. 064322.

(41) Zamanipour, Z.; Shi, X.; Dehkordi, A. M.; Krasinski, J. S.; Vashaee, D. The effect of synthesis parameters on transport properties of nanostructured bulk thermoelectric p-type silicon germanium alloy. *phys. status solidi (a)* **2012**, *209*, 2049−2058.

(42) Horák, J.; Cermak, K.; Koudelka, L. Energy formation of antisite defects in doped Sb2Te3 and Bi2Te3 crystal. *J. Phys. Chem. Solids* **1986**, *47*, 805−809.

(43) Kumar, S.; Singh, S.; Dhawan, P. K.; Yadav, R. R.; Khare, N. Effect of graphene nanofillers on the enhanced thermoelectric properties of Bi2Te3 nanosheets: elucidating the role of interface in de-coupling the electrical and thermal characteristics. *Nanotechnology.* **2018**, *29*, No. 135703.

(44) Agarwal, K.; Kaushik, V.; Varandani, D.; Dhar, A.; Mehta, B. R. Nanoscale thermoelectric properties of Bi2Te3 − Graphene nanocomposites: Conducting atomic force, scanning thermal and kelvin probe microscopy studies. *J. Alloys Compd.* **2016**, *681*, 394−401.

(45) Hooshmand Zaferani, S.; Ghomashchi, R.; Vashaee, D. Strategies for engineering phonon transport in Heusler thermoelectric compounds. *Renewable Sustainable Energy Rev.* **2019**, *112*, 158−169.

(46) Ferry, D. K. *Semiconductor Transport*; Taylor & Francis: London, 2000.

(47) Mahan, G. D.; Bartkowiak, M. Wiedemann−Franz law at boundaries. *Appl. Phys. Lett.* **1999**, *74*, 953.

(48) McKinney, R. W.; Gorai, P.; Stevanovi′c, V.; Toberer, E. S. Search for new thermoelectric materials with low Lorenz number. *J. Mater. Chem. A.* **2017**, *5*, 17302−17311.

(49) Li, M.; L.Cortie, D. L.; Liu, J.; Yu, D.; Kazi NazrulIslam, S. M.; Zhao, L.; Mitchell, D. R. G.; A.Mole, R. A.; Cortie, M. B.; Dou, S.; Wang, X. Ultra-high thermoelectric performance in graphene incorporated Cu2Se: Role of mismatching phonon modes. *Nano Energy* **2018**, *53*, 993−1002.

(50) Zhao, D.; Wang, X.; Wu, D. Enhanced Thermoelectric Properties of Graphene/Cu2SnSe3 Composites. *Crystals* **2017**, *7*, 71.

(51) Yue, H.; Yao, L.; Gao, X.; Zhang, S.; Guo, E.; Zhang, H.; Lin, X.; Wang, B. Effect of ball-milling and graphene contents on the mechanical properties and fracture mechanisms of graphene nanosheets reinforced copper matrix composites. *J. Alloys Compd.* **2017**, *691*, 775−762.

(52) Hu, X.; Chan, Y. C.; Zhang, K.; Yung, K. C. Effect of graphene doping on microstructural and mechanical properties of Sn−8Zn−3Bi solder joints together with electromigration analysis. *J. Alloys Compd.* **2013**, *580*, 162−171.

(53) Yan, S. J.; Dai, S. L.; Zhang, X. Y.; Yang, C.; Hong, Q. H.; Chen, J. Z.; Lin, Z. M. Investigating aluminum alloy reinforced by graphene nanoflakes. *Mater. Sci. Eng. A* **2014**, *612*, 440−444.

(54) Taha, A. S.; Hammad, F. H. Application of the Hall-Petch Relation to Microhardness Measurements on Al, Cu, Al-MD 105, and Al-Cu Alloys. *phys. status solidi (a).* **1990**, *119*, 455.

(55) Bhadauria, A.; Singh, L. K.; Laha, T. Effect of physiochemically functionalized graphene nanoplatelet reinforcement on tensile properties of aluminum nanocomposite synthesized via spark plasma sintering. *J. Alloys Compd.* **2018**, *748*, 783−793.

(56) Shin, S. E.; Bae, D. H. Deformation behavior of aluminum alloy matrix composites reinforced with few-layer graphene. *Composites, Part A* **2015**, *78*, 42−47.

(57) Hooshmand Zaferani, S. Improvement if Thermoelectric Properties Through Manipulation of Microstructure: Effect of Graphene Reinforcement. PhD Project, School of Mechanical Engineering, The University of Adelaide: Australia.

(58) Rashad, M.; Pan, F.; Zhang, J.; Asif, M. Use of high energy ball milling to study the role of graphene nanoplatelets and carbon nanotubes reinforced magnesium alloy. *J. Alloys Compd.* **2015**, *646*, 223−232.

(59) Zhang, T.; J, S.; LÜ, L.-q.; Wang, C.-m.; Sang, J.-x.; Wu, D. Effects of graphene nanoplates on microstructures and mechanical properties of NSA-TIG welded AZ31 magnesium alloy joints. *Trans. Nonferrous Met. Soc. China* **2017**, *27*, 1285−1293.

(60) Rashad, M.; Pan, F.; Asif, M. Exploring mechanical behavior of Mg−6Zn alloy reinforced with graphene nanoplatelets. *Mater. Sci. Eng. A* **2016**, *649*, 263−269.

(61) Rowe, D. M. *Thermoelectrics and Its Energy Harvesting, Modules, Systems, AndApplications in Thermoelectrics*; CRC Press-Taylor & Francis Group: New york, 2012 © 2012 byTaylor & Francis Group, LLC, ISBN:978-1-4665-6030-7.

(62) Meng, Z.; Soler-Crespo, R. A.; Xia, W.; Gao, W.; Ruiz, L.; Espinosa, H. D.; Keten, S. A coarse-grained model for the mechanical behavior of graphene oxide. *Carbon* **2017**, *117*, 476−487.

(63) Yin, H.; Qi, H. J.; Fan, F.; Zhu, T.; Wang, B.; Wei, Y. Griffith Criterion for Brittle Fracture in Graphene. *Nano Lett.* **2015**, *15*, 1918−1924.

(64) Chung, J.-Y.; Sorkin, V.; Pei, Q.-X.; Chiu, C.-H.; Zhang, Y.-W. Mechanical properties and failure behaviour of graphene/silicene/graphene heterostructures. *J. Phys. D: Appl. Phys.* **2017**, *50*, No. 345302.

(65) Mefford, C. H.; Qiao, Y.; Salviato, M. Failure behavior and scaling of graphene nanocomposites. *Compos. Struct.* **2017**, *176*, 961−972.

(66) Hooshmand Zaferani, S.; Darebaghi, A.; Hong, S.; Vashaee, D.; Ghomashchi, R. Experimental Realization of Heavily p-doped Half-Heusler CoVSn Compound. *Energies* **2020**, *13*, No. 1459.

(67) Ghodrati, H.; Ghomashchi, R. Effect of Graphene Dispersion and Interfacial bonding on the Mechanical Properties of Metal Matrix Composites: An Overview. *FlatChem* **2019**, *16*, No. 100113.

(68) Cao, H.; Liang, Y. The microstructures and mechanical properties ofgraphene-reinforced titanium matrix composites. *J. Alloys Compd.* **2020**, *812*, No. 152057.